

# Bend stiffness of laminate microstructures containing three dissimilar materials

Damiano Pasini

Received: 14 July 2008 / Accepted: 1 December 2008  
© Springer Science+Business Media, B.V. 2008

**Abstract** This article examines the effective flexural modulus of a multilayered micro-system evolving into alternative layered structures consisting of three dissimilar materials. A multiscale model of the bending stiffness is presented to capture the impact of changing the constituent materials, the layer architecture and the cross-section geometry. The results are plotted onto maps to show the existence of specific domains, within which fall the effective properties of all possible tri-material multilayered configurations. The potential to stiffen a bi-material system is demonstrated by integrating additional layers of a more flexible material for given constraints on the volume fraction. The proposed scheme is conducive to contrast structural alternatives in constrained and unconstrained design. A case study shows how the maps enable optimum selection among various design concepts, which may range from monolithic materials with alternative shape geometries to systems consisting of two and three materials arranged in dissimilar multiple layer architectures.

**Keywords** Multilayered system ·  
Flexural modulus modelling ·  
Layer geometry and material selection

---

D. Pasini (✉)  
Department of Mechanical Engineering, Institute  
for Advanced Materials of McGill University,  
817 Sherbrooke Street West, Montreal, QC,  
Canada H3A2K6  
e-mail: damiano.pasini@mcgill.ca

## Notations

$A$	Cross sectional area
$B$	Width (m)
$b$	Internal width (m)
$c$	Dimensionless multiplier of cross-section internal width ( $c = b/B$ )
$c_1$	Beam curvature
$d$	Dimensionless multiplier of cross-section internal height ( $d = h/H$ )
$D$	Rectangular cross-section envelope
$E$	Young's modulus (GPa)
$E_D, \rho_D$	Effective of properties of prismatic beam
$E_T, \rho_T$	Effective of properties of shaped beam
$h$	Internal height (m)
$H$	Height (m)
$I$	Second moment of area (m <sup>4</sup> )
$J_T$	Cross-section torsional constant (m <sup>4</sup> )
$l$	Beam length (m)
$M_b$	Bending moment per unit width
$m$	Mass (mg)
$n$	Exponent of Lamé' curves
$p$	Performance index
$q$	Scaling parameter of performance index
$r_g$	Radius of gyration (m)
$u, v$	Envelope multipliers
$S$	Shape
$V$	Volume (m <sup>3</sup> )
$\rho$	Material density (mg/m <sup>3</sup> )
$\lambda$	Envelope efficiency parameter
$\psi$	Shape transformer

## 1 Introduction

Compared to monolithic materials, multilayered shaped structures have the potential to boost the performance of the next generation of micro-devices. The physical properties of these composites can be tailored to obtain optimized mechanical performance, often unachievable with the use of a single material. As monolithic structures, multilayered systems can work as transducers and, thus, be used in a large number of applications. For example, they are able to sense voltage, measure force and acceleration, move and control mechanisms, detect variations in current, pressure, temperature and other physical properties (Gad-el-Hak 2002; Senturia 2001; de Silva 2007). Such capacities of sensing and actuation can be exploited in biotechnology (Wang and Soper 2006), telecommunication and aerospace control (Gad-el-Hak 2002; Senturia 2001; de Silva 2007), for the design of gyroscope (Degani et al. 1998; Hong et al. 2000) and wireless antenna (Nguyen et al. 1998; Nguyen 2004; Sova and Bogdan 2003), micromechanical mixer-filters (Nguyen 1999; Wong and Nguyen 2004; Nguyen 1995), radio transmitters and receivers (Galayko et al. 2005; Huang et al. 2002), Atomic Force Microscope probes (Sader 1998; Serre et al. 1999) and piezoelectric biosensors (Rasmussen et al. 2003; Jennifer et al. 2004; Taka et al. 1993; Lange et al. 2002; Thaysen et al. 2002; Cheggour et al. 2005; Marie et al. 2002; Khaled et al. 2003; Yue et al. 2004).

Whereas in the past the design of micro-devices was confined to a single material, mainly Silicon, and to simple geometries, generally prismatic, recent advances in micromachining technology enable the manufacture of optimized micro-structures consisting of multimaterials shaped in more efficient geometries (Lin 2004a, b; Ferguson et al. 2005; Sandberg et al. 2005a, b, c; Mertens et al. 2003). For instance, multimaterial structures can be machined into complex shapes by using non-contact processes, e.g. laser technology, which can directly etch away unwanted material with high precision.

The sensitivity to bending motion generally plays a crucial role in the functioning of a micro-beam. It is governed by the flexural modulus and for some applications it is one of the most important properties. For example, the bending stiffness is essential in a range of applications that require the transducer to comply to a prescribed deformation, to actuate force,

to store elastic energy, as well as to vibrate at a certain frequency (Huber et al. 1997; Melamud et al. 2006; Shieh et al. 2001; Spearing 2000; Vengallatore and Spearing 2003).

Both materials and geometry have a strong impact on the bending stiffness as well as on other mechanical properties, e.g. ductility, damping and strength, of a multi-laminate structure consisting of different materials. The effective properties depend on the material attributes of each layer, and on the geometry, which is governed by variables describing form and length of the element, shape and size of the cross-section, number and stacking sequence of the layers as well as their configuration (Ashby 1993a; Pasini 2006; Smith and Partbridge 1999; Pasini et al. 2003). The geometric variables combined with the material properties specify the building blocks of a structural concept and, thus, strongly impact the functioning of a micro-device (Cox 1965; Shanley 1960; Caldwell and Woodhead 1973; Parkhouse 1984; Ashby 1991, 1993b, 1999; Pasini 2006b).

In different areas of applied mechanics it has been demonstrated that optimizing the performance of a structural concept requires a simultaneous selection of the variables pertaining to its geometry and materials. Different models have been proposed in the past to ease the search for the best concept of a given application. However, such methods can only model certain geometric variables at one scale (Pasini et al. 2003; Cox 1965; Shanley 1960; Caldwell and Woodhead 1973; Parkhouse 1984; Ashby 1991, 1993b, 1999; Pasini 2006; Rakshit and Ananthasuresh 2008). This article proposes a multiscale scheme for simultaneous selection of constituent materials, layers arrangement, and cross-section geometry in constrained and unconstrained beam design. The geometry is considered at two scale levels. At a lower level of the layer architecture, the variables describing the geometry are those related to the way laminates are nested or stacked in series, to the symmetry and number of layers, as well as the volume fraction of each material. At a higher level, the variables are those that capture relative changes in the cross-section geometry, e.g. size, shape and symmetry. The method is used to develop design maps that are conducive to the selection of structural alternatives for a given bending stiffness requirement.

In Sect. 2, this article illustrates the evolution of a generic three-material system into different

multilayered architectures. Section 3 describes the method used to characterize the structural geometry at two scales of the structural hierarchy. In Sect. 4, the flexural modulus of a generic multilaminate is formulated as a function of material attributes, layer arrangement and cross-section geometry. The results are visualized in Sect. 5 on maps that illustrates minimum and maximum bounds of the stiffness domain. A case study closing the paper shows the use of the charts for co-selecting structural and material variables in constrained and unconstrained design.

## 2 The evolution of multilayered systems consisting of three materials

A recent study on the vibration response of a multilayered microresonator has demonstrated that for a bi-material system the flexural modulus of all possible layers configurations is bounded by two curves (Pasini 2006a). The lower represents three symmetric vertically scaled layers with a low Young's modulus core. The upper one describes the same layer configuration but with the stiffer material in the middle. All the other bi-material configurations evolving in multiple symmetric or asymmetric layers, such as those consisting of five, seven, nine, and even more laminates, fall into the stiffness domain. Starting from this result, this article examines a tri-material laminated micro-structure evolving from a bi-material system. Examples of the system evolutions considered in this article are shown in Fig. 1. The purpose here is to explore how the flexural modulus changes when a third dissimilar material of increasing thickness is integrated into the bi-material structure with respect to given constraints on its volume fraction.

The structural concepts shown in Fig. 1 are governed by the way in which layers are scaled with respect to each other within the envelope, regardless of their number, symmetry and thickness. Such concepts are pertinent to micro-structural design because of their practical use, manufacturability, and potential performance. In Fig. 1, the concepts are grouped into three classes identified by the relative scaling of the layers, namely vertically, proportionally, and horizontally scaled layers. Within each class, we focus on the system evolutions that respect two constraints applied to the volume fraction of the

constituents. In the first scenario, a constraint is imposed on the volume fraction of the external material, which, as a result, remains fixed. Here, it is the volume fraction of the third material that increases by thickening the layer either in the middle (Fig. 1a) or at the interface with the first material (b). The bi-material  $M_1$ – $M_2$  evolves in a tri-material composite (1–2–3) until  $M_2$  vanishes and is replaced by  $M_3$ . The second scenario, on the other hand, involves constraining the volume fraction ratio of  $M_1$  and  $M_2$  such that  $V_1/V_2 = \text{const}$ . In this case, the bi-material evolves into a three-material system, following either pattern (c) or (d) until the final configuration, in which the system has become monolithic.

Likewise, the same evolutions a) to d) can be applied to the other two layer architectures of Fig. 1, although displayed are only those corresponding to (a) and (c), where  $M_2$  is in the middle.

## 3 Modelling geometric properties

This section describes the scheme that will be used to model the flexural modulus and the density (Pasini 2006a, b). The method is based on a shape classification that allows the structural variables to be identified at both the levels of the cross-section and the material layers.

### 3.1 Classifying shapes

Although theoretical, shape families and their classes can help contrast structural candidates at the concept stage. Here, the term *family* describes a shape concept for the cross-section regardless of its size, such as the rectangular or circular cross-sections. Within a family, fall all the solid shapes with same contour as well as their derived hollow shapes, where the internal contour is described by the same function as the external contour, as illustrated in Fig. 2a. Shapes of a family can then be categorized into classes. The term *class* refers to the layer architecture, which involves the way layers are scaled with respect to each other within a given cross-section, as shown in Fig. 1.

The general expression of the superellipses, described by the Lamé' curves is used to describe the shape contour defining a family. The implicit form of the Lamé' curves with positive radii  $B/2$  and  $H/2$  and  $n$  any rational number is given by

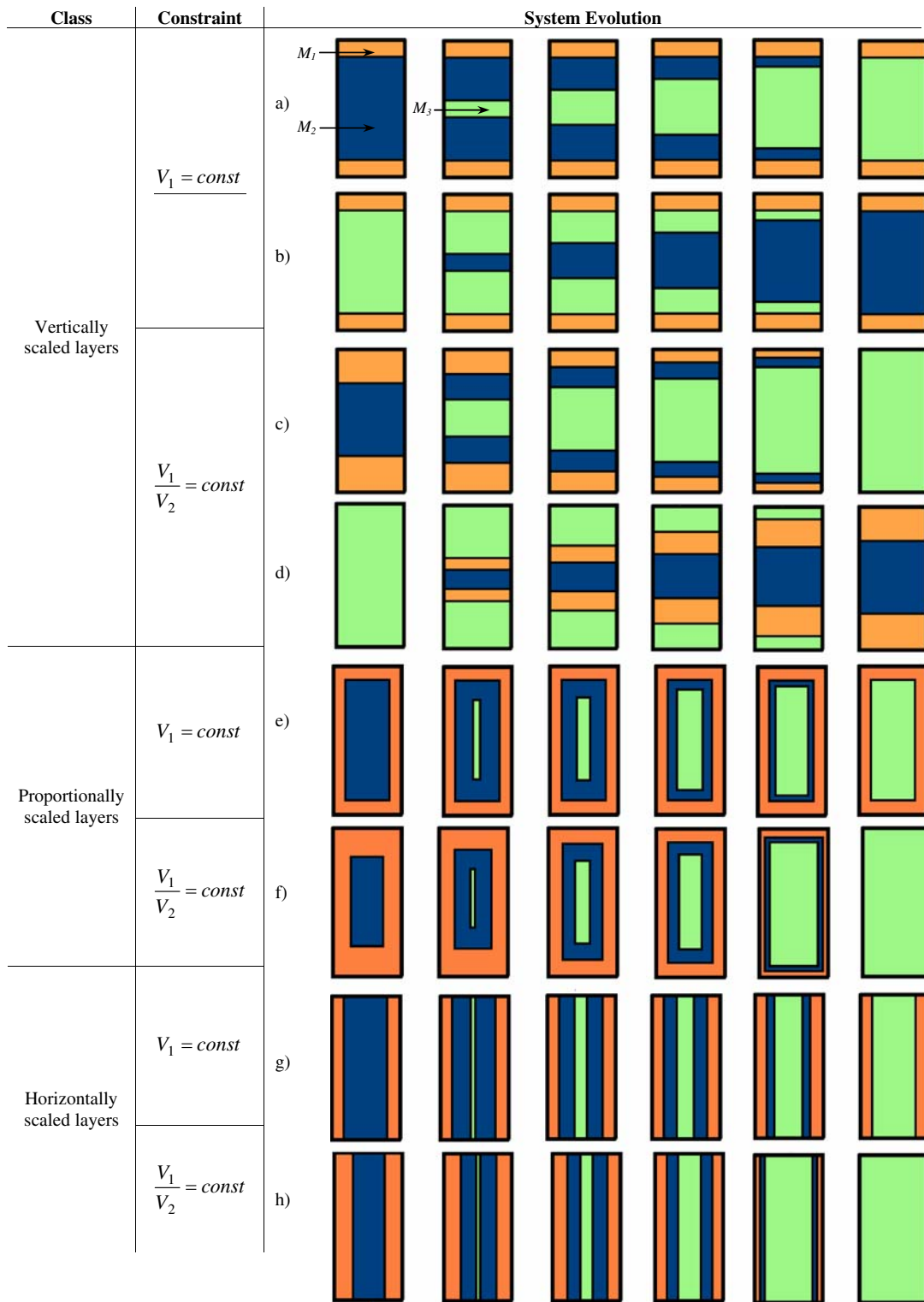
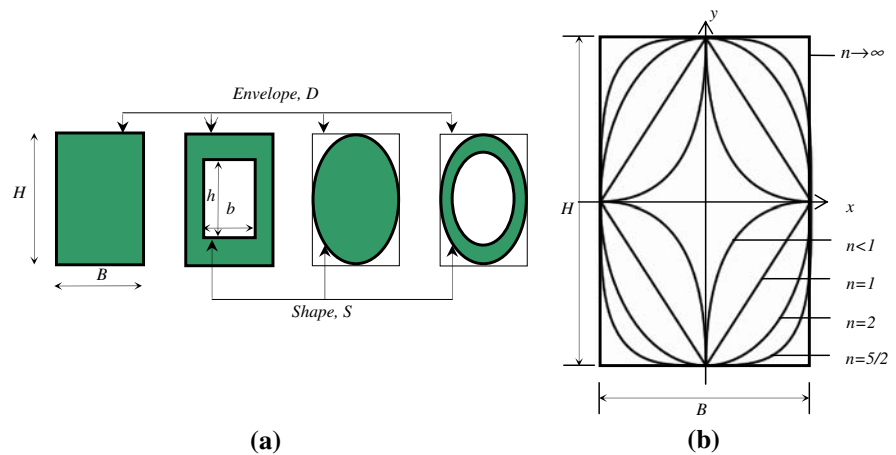


**Fig. 1** Evolution of a bi-material system into alternative three-material systems

**Fig. 2** **a** Cross-sections of the rectangular and ellipse families; **b** Superelliptical shapes governed by the power  $n$  of the Lamé' curves



$$\left| \frac{x}{B/2} \right|^n + \left| \frac{y}{H/2} \right|^n = 1 \quad (1)$$

Figure 2b shows Lamé' curves plotted for different values of  $n$ . These are smooth profiles whose form is determined by the exponent  $n$ . Although nine types of Lamé' curves can be defined, here we consider only the subset of Lamé' curves, where  $n$  is a positive integer. In this case, when  $n = 2$ , Eq. (1) represents an ellipse, whereas for  $n > 2$ , the curve becomes a superellipse until it is a rectangle for  $n \rightarrow \infty$ . If  $n < 2$ , we obtain hypoellipses with sharp corners at the  $x$  and  $y$  axes.

In this work, the power  $n$  of the Lamé' curves is used to sort shapes into families regardless of shape size. With respect to  $n$ , an infinite number of shape families can be obtained. Some of them are shapes for which we have proper names, such as the ellipse family for  $n = 2$ , the diamond family for  $n = 1$ , as well as the rectangle family for  $n \rightarrow \infty$  (Table 1). Others are not associated with a definite name but are still families identified by the specific power of their defining superellipse. Besides solid shapes, hollow shapes fall into a family if the internal and the external contours are governed by the same power  $n$  of the Lamé' curves. The internal layers may either be filled with materials or be empty.

The architecture of the internal layers permits the shapes of a family to be categorized into three classes, as shown in Fig. 1. Classes can be applied to any family and to create them we use the scaling relation between the internal layers and the external contour. Three scaling modes are considered here, one for each class. In the first one fall all the shapes with the same relative vertical scaling between the

internal and external contours. To the second belong shapes which have proportionally scaled layers. The third class emerges when a horizontal scaling governs the layer architecture.

### 3.2 Geometric parameters

Since cross-sections may differ for their size and shape, we introduce parameters that can capture relative changes of size independently on those of shape. To describe the former, which involves cross-section scaling, we introduce a real entity, referred as the envelope  $D$ . This is specified by the rectangle of equal dimension of its cross-section size (Fig. 2a). The latter, on the other hand, describes the cross-section contour,  $S$ , enclosed in  $D$ , and it is characterized by dimensionless properties, named *shape transformers*.

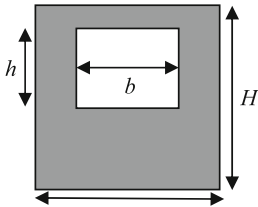
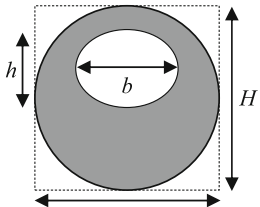
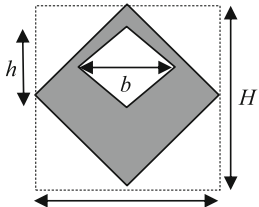
#### 3.2.1 Scaling

The scaling relations of a generic envelope ( $B$ ,  $H$ ) relative to a reference solid rectangle ( $B_o$  and  $H_o$ ) can be simply defined by two linear multipliers  $u = \frac{B}{B_o} = \frac{b}{B}$  and  $v = \frac{H}{H_o} = \frac{h}{H}$ , where  $b$  and  $h$  are the internal dimensions of a hollow cross-section (Tables 1 and 2).

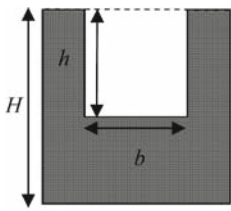
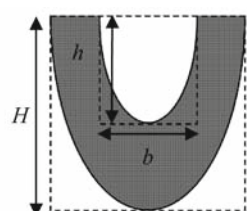
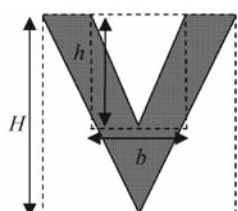
#### 3.2.2 Shape properties

The shape properties of the figure enclosed in  $D$  can be described by dimensionless shape transformers. These are defined by normalizing a geometric quantity,  $g$ , of

**Table 1** Shape transformers for double symmetry axes shape families ( $c = b/B$ ,  $d = h/H$ )

<p>The Rectangles Family</p>  <p><math>n = \infty</math></p>	<p>The Ellipses Family</p>  <p><math>n = 2</math></p>	<p>The Diamonds Family</p>  <p><math>n = 1</math></p>
$\psi_A = \beta_1[1 - cd]$ $\beta_1 = 1$ $0 \leq \psi_A \leq 1$ $\psi_I = \beta_2$ $\beta_2 = 1$ $0 \leq \psi_I \leq 1$ $PA = \beta_3 \left[ cd \left( \frac{1 - cd(2d_1 + d)}{2(1 - cd)} - d_1 - \frac{d}{2} \right)^2 \right]$ $\beta_3 = 12$ $\lambda_I = \beta_4 \left[ (1 - cd^3 - PA)(1 - cd)^{-1} \right]$ $\beta_4 = 1$ $1 \leq \lambda_I \leq 3$	$\beta_1 = \frac{\pi}{4}$ $0 \leq \psi_A \leq \frac{\pi}{4}$ $\beta_2 = \frac{3\pi}{16}$ $0 \leq \psi_I \leq 0.588$ $\beta_3 = \frac{3}{4}$ $\beta_4 = \frac{3}{4}$ $\frac{3}{4} \leq \lambda_I \leq \frac{9}{4}$	$\beta_1 = \frac{1}{2}$ $0 \leq \psi_A \leq \frac{1}{2}$ $\beta_2 = \frac{1}{4}$ $0 \leq \psi_I \leq \frac{1}{4}$ $\beta_3 = \frac{1}{2}$ $\beta_4 = \frac{1}{2}$ $\frac{1}{2} \leq \lambda_I \leq \frac{3}{2}$

**Table 2** Shape transformers for families with single symmetry axis shape  $\psi_A = \beta_1[1 - cd]$ 

 <p><math>n = \infty</math></p>	 <p><math>n = 2</math></p>	 <p><math>n = 1</math></p>
$\psi_A = \beta_1[1 - cd]$ $\beta_1 = 1$ $0 \leq \psi_A \leq 1$ $\psi_I = \beta_2[1 - cd^3 - PA]$ $\beta_2 = 4$ $0 \leq \psi_I \leq 1$ $PA = \beta_3 \left[ (cd^2 - 1)^2 (1 - cd)^{-1} \right]$ $\beta_3 = \frac{3}{4}$ $\lambda_I = \beta_4 \left[ (1 - cd^3 - PA)(1 - cd)^{-1} \right]$ $\beta_4 = 4$ $0 \leq \lambda_I \leq \frac{5}{4}$	$\beta_1 = \frac{\pi}{4}$ $0 \leq \psi_A \leq \frac{\pi}{4}$ $\beta_2 = \frac{3\pi}{4}$ $0 \leq \psi_I \leq 0.690$ $\beta_3 = 0.720$ $\beta_4 = 3$ $0.350 \leq \lambda_I \leq 1.14$	$\beta_1 = \frac{1}{2}$ $0 \leq \psi_A \leq \frac{1}{2}$ $\beta_2 = 1$ $0 \leq \psi_I \leq \frac{1}{3}$ $\beta_3 = \frac{2}{3}$ $\beta_4 = 2$ $\frac{1}{2} \leq \lambda_I \leq 1$

a cross-section by the same geometric quantity,  $g_D$ , of its solid rectangular envelope as:

$$\psi_g = \frac{g}{g_D} \quad (2)$$

For example, relation (2) can be used to express respectively the shape properties of the area, the second moment of area about the x axis, and the torsional constant, as

$$\begin{cases} \psi_A = \frac{A}{A_D} \\ \psi_{I_{xx}} = \frac{I_{xx}}{I_D} \\ \psi_{J_T} = \frac{J_T}{J_{TD}} \end{cases} \quad (3)$$

Tables 1 and 2 give the expressions of the shape transformers for three families for double axis and single axis symmetry shapes respectively.  $\psi_A$  and  $\psi_I$  play a similar role as the material properties, since they are independent of size changes. In addition alike materials, shape families and classes exhibit properties that fall into a particular range, whose values vary with respect to the amount of area filling the shape. For monolithic system when the material completely saturates the shape,  $\psi_g$  assumes the upper bound of the range; whereas for hollow shapes,  $\psi_g$  decreases with respect to the filling material until reaching the lower bound, which corresponds to an empty shape. It is noted that, although theoretical, shape classes can be identified for each shape family, as shown in Figs. 3 and 4.

For monolithic, uniform and isotropic materials, the ratio  $\lambda_I = \psi_I/\psi_A$  provides a measure of the

geometric contribution a shape can provide to the flexural stiffness of a cross-section, regardless of its size. The higher the value of  $\lambda_I$ , the stiffer in bending as well as lighter the shape is. The ranges of such shape potential are shown in Figs. 3 and 4. However, these are theoretical values which do not consider manufacturing constraints, shear and buckling failure requirements. Nevertheless, they are helpful for preliminary comparisons of structural concepts.

Shape transformers and envelope multipliers allow to re-formulate the equations of mechanics in terms of four factors as  $F, M, \psi_g, g_D$  where  $F$  describes the functional requirements,  $M$  the material properties,  $\psi_g$  and  $g_D$  the cross-section geometry decoupled respectively in shape and size (Pasini 2006a, b; Pasini et al. 2003). When possible, such a formulation permits the co-selection of material and shape in constrained and unconstrained design. This rationale is applied in the following sections to examine the flexural modulus of a three-material multilayered system.

#### 4 Flexural modulus of a three materials multilayered micro-system

To characterize the flexural modulus of a three-material system, we consider the material properties of the layers, the shape and the size of the cross-section, the architecture and the number of the layers as design variables. The model presented here is based on the Classic Laminated Plate Theory (CLPT), which assumes the resulting strain and curvatures are uniform throughout the layers. Since

**Fig. 3** Range of shape transformers for the three shape classes of each family

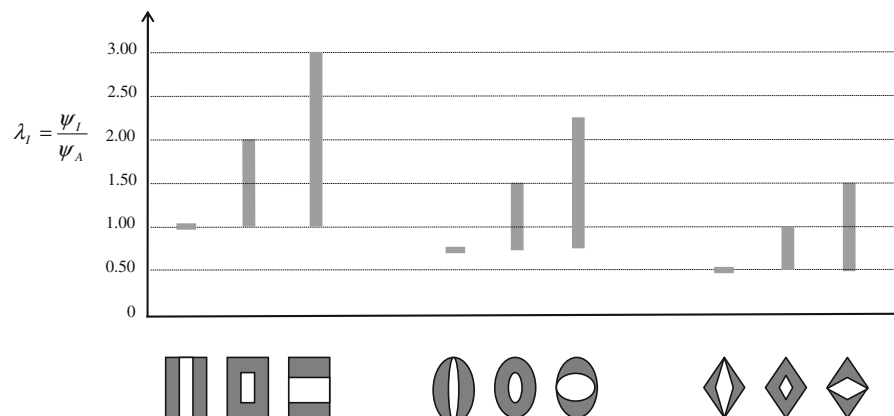
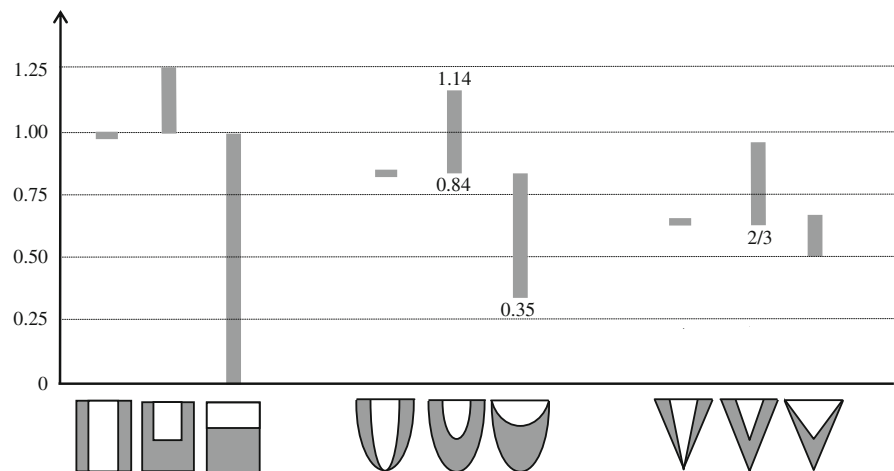




**Fig. 4** Range of shape transformers for shape classes



micro-systems are integrated composite structures where materials can be processed by using different techniques, it is essential to consider the issues of layer adhesion and the mechanisms that develop intrinsic and thermo-mechanical stresses. Depending on the manufacturing process, the interfaces and their properties certainly impact the effective mechanical response of the system. As in previous works (Ferguson et al. 2005; Sandberg et al. 2005a, b, c; Pasini 2006a), the model presented here is based on the assumption that there is a perfect bonding between each layer. Although this hypothesis is too unrefined for the detailed stage of design, it still fits the purpose of a preliminary selection of the constituent materials since it allows find limiting ideal bounds of the effective properties. Further work is required to include the effects of the interfacial stresses on the design maps presented in this article. Besides this assumption, the strain at the interface between materials is also assumed to remain unchanged. Bending strain is assumed to vary linearly along all the layers with no discontinuity. The stress, on the other hand, is continuous only within each layer, but it is discontinuous at the layer transition, since each material has its own moduli. These simplifications are ideal and can be accepted at a preliminary stage of design. In reality, the production process used to multilayer the micro-structure creates non-planarity between layers. Interatomic interactions, ledges, dislocations and other interface characteristics affect the degree of interfacial adhesion between layers. An interfacial surface is usually

introduced to characterize the effects of interfaces in thin layers (Spaepen 2000; Yang et al. 2002). Another assumption concerns the micro-structure size, which should be greater than  $1\text{ }\mu\text{m}$  to satisfy the laws of continuum mechanics. Therefore, in this article we limit ourselves to the case of microstructure of at least  $1\text{ }\mu\text{m}$  size and slenderness aspect ratio in the range 1:10–1:20. Furthermore, the microbeam has a uniform cross section along its axis, is loaded in its plane of symmetry and undergoes only small deformation satisfying the Euler–Bernoulli theory. Length and boundary conditions are prescribed. We consider the stiffness to mass ratio as a criterion to contrast micro-beam concepts. For the material properties, we assume conservative values, which are represented by the bulk homogeneous isotropic attributes (Vengallatore and Spearing 2003; Pasini 2006a). These assumptions, extensively used especially in literature for vibration analysis, were verified to yield results that do not diverge more than 3% from experimental measures (Wang and Soper 2006; Degani et al. 1998; Hong et al. 2000; Nguyen et al. 1998; Nguyen 2004; Lin 2004a, b; Ferguson et al. 2005; Sandberg et al. 2005a, b, c; Mertens et al. 2003; Melamud et al. 2006; Wang et al. 2000).

We examine first the variables at the level of the layer architecture before moving to the cross-section geometry. For this purpose, the beam is assumed prismatic with dimensions  $B$ ,  $H$  and  $l$ , and a cross-section reference of properties  $\psi_A = \psi_I = 1$  (Table 1). The beam subjected to a pure bending moment  $M_B$  per unit width may consist of multiple



material layers arranged with respect to the shape classes. The flexural stiffness and unit mass of the system can be simplified as follows

$$\frac{M_B}{c_1} = \psi_I I_D E_D = I_D E_D \quad (4)$$

$$\frac{m}{l} = \psi_A A_D \rho_D = A_D \rho_D \quad (5)$$

where  $c_1$  is the curvature of the prismatic beam.  $\frac{M_B}{I_D c_1} = E_D$  and  $\frac{m}{A_D l} = \rho_D$  are respectively the effective properties, flexural modulus and density, of the beam. To express them as a function  $f()$  of the layer geometry,  $L_g$ , and their materials, we assign to the  $i$ th layer, where  $i = 1, 2, \dots, k$ , Young's Modulus and density  $E_i$  and  $\rho_i$ , respectively, and second moment of area and area  $I_i$  and  $A_i$ . Then, we express the geometry of the layer architecture in terms of the shape transformers of each layer,  $\psi_{Ai}$  and  $\psi_{Ii}$ , and write the effective properties of the system as

$$E_D = \sum_{i=1}^k E_i \frac{I_i}{I_D} = \sum_{i=1}^k E_i \frac{\int_{A_i} y_i^2 dA}{I_D} = \underbrace{\sum_{i=1}^k E_i \psi_{Ii}}_{f(L_g)} \quad (6)$$

$$\rho_D = \sum_{i=1}^k \rho_i \frac{A_i}{A_D} = \underbrace{\sum_{i=1}^k \rho_i \psi_{Ai}}_{f(L_g)} \quad (7)$$

Having modelled the properties at the level of the layers, the focus is now on the next level of the structural hierarchy, i.e. the cross-section geometry. We consider a beam of generic cross-section shape,  $S$ , which can have either a double axis or single axis symmetry, as shown in Tables 1 and 2. The transformed flexural modulus and density can be obtained by rearranging expressions (4) and (5), and by applying  $\psi_A \neq 1$  and  $\psi_I \neq 1$  to their respective properties of the envelope,  $E_D$  and  $\rho_D$ , as

$$E_T = \frac{M_B}{c_1 I_D^2} = \psi_I E_D = \underbrace{\psi_I}_{S} \underbrace{\sum_{i=1}^k E_i \psi_{Ii}}_{f(L_g)} \quad (8)$$

$$\rho_T = \frac{m}{l A_D^2} = \psi_A \rho_D = \underbrace{\psi_A}_{S} \underbrace{\sum_{i=1}^k \rho_i \psi_{Ai}}_{f(L_g)} \quad (9)$$

The above effective properties can capture the multiscale effect of changing the variables at

different levels of the structural hierarchy. The relations give design freedom to choose concurrently the basic materials from the bulk material list, the layer architecture  $f(L_g)$  from the shape classes, which are assumed to guarantee the perfect bond of the layers, and the cross-section shape  $S$  from the shape families. In addition, the normalized model allows variable selection without the need of knowing the spring constant, which is a requirement prescribed by the problem. Section 6 presents a case study illustrating the impact of changing simultaneously the variables at both the levels of the cross-section geometry and of the layer architecture.

The ratio of Eqs. (8) and (9) is a metric relevant to the design of a resonating beam, because it is representative of the capacity of storing energy, of the resonance frequency and, to the first order, of the actuation speed. If besides length and boundary conditions, also the sizes of the micro-beam are prescribed, then the ratio  $p$  of relations (8) and (9) simplify to:

$$p = \frac{E_T}{\rho_T} = \lambda_I \frac{E_D}{\rho_D} \quad (10)$$

For a prescribed envelope, the higher the value of  $p$ , the higher the vibration frequency, the better the capacity to store elastic energy, and the stiffer as well lighter is the beam. On the other hand, when the cross-section is free to be scaled and the designer chooses to scale the envelope in a particular direction, then  $p$  can be expressed by the general form:

$$p = \frac{E_T}{\rho_T} = \frac{\left( \psi_I \sum_{i=1}^k E_i \psi_{Ii} \right)^q}{\psi_A \sum_{i=1}^k \rho_i \psi_{Ai}} \quad (11)$$

where  $q = \ln uv / \ln uv^3$  is the scaling parameter which assumes values ranging from  $-\infty$  to  $+\infty$  (Pasini 2006b). As a function of  $u$  and  $v$ ,  $q$  is governed by the direction along which a cross-section can be scaled. Reasons for selecting a given direction of scaling have been explored in material design (Pasini et al. 2003; Pasini 2006b). In general, a designer has to either respect applied geometric constraints or choose a direction that maximizes certain performance criteria for a given load.

Three types of geometric scaling constraints are considered here for their frequent use in structural

design. The first occurs when the envelope is subjected to a height constraint, which entails horizontal scaling, described by  $v = 1$ . The second one is proportional scaling, where  $u = v$ , usually applied in an unconstrained design space where all dimensions can be uniformly scaled. Finally,  $u = 1$  describes a vertical direction of scaling, usually enforced to constraint the width. In these three cases, the scaling parameter becomes a constant, regardless of materials, shape attributes and layer architecture. Thus, relation (11) can be simplified to:

$$p = \lambda \frac{E_D}{\rho_D} \text{ for horizontal scaling} \quad (12)$$

$$p = \frac{(\psi_I E_D)^{1/2}}{\psi_A \rho_D} \text{ for proportional scaling} \quad (13)$$

$$p = \frac{(\psi_I E_D)^{1/3}}{\psi_A \rho_D} \text{ for vertical scaling} \quad (14)$$

Rearranging and taking the log of Eq. (11) leads to plot selection guidelines for a given scaling direction. From (11), the general expression of an iso-performance line is given by:

$$\log E_T \psi_I = \frac{1}{q} \log \rho_T \psi_A + \frac{1}{q} \log p \quad (15)$$

When the direction of scaling is set a priori, then the parameter  $q$  is known and expressions (12), (13) and (14), rearranged as in (15) can be plotted on maps for the co-selection of material, cross-section geometry and layer architecture. This is shown in the next sections.

## 5 Maps characterizing the effective flexural modulus and density of a multilayered system

In expression (11), the variables capture structural characteristics at three levels of the structural hierarchy: material, layer architecture and cross-section geometry. The effective flexural modulus and density of a multilaminated structure  $C$  can be illustrated on a map of  $\rho_T$  vs.  $E_T$  by the coordinates  $C(\rho_T, E_T)$ . The property ratio  $E_T/\rho$  is the slope of the line passing through  $C$  and the origin of the plot. The greater the slope, the higher the performance.

The maps presented in this work assist the preliminary stage of microstructure design. The

**Table 3** Material properties of candidate structures (Sharpe 2001)

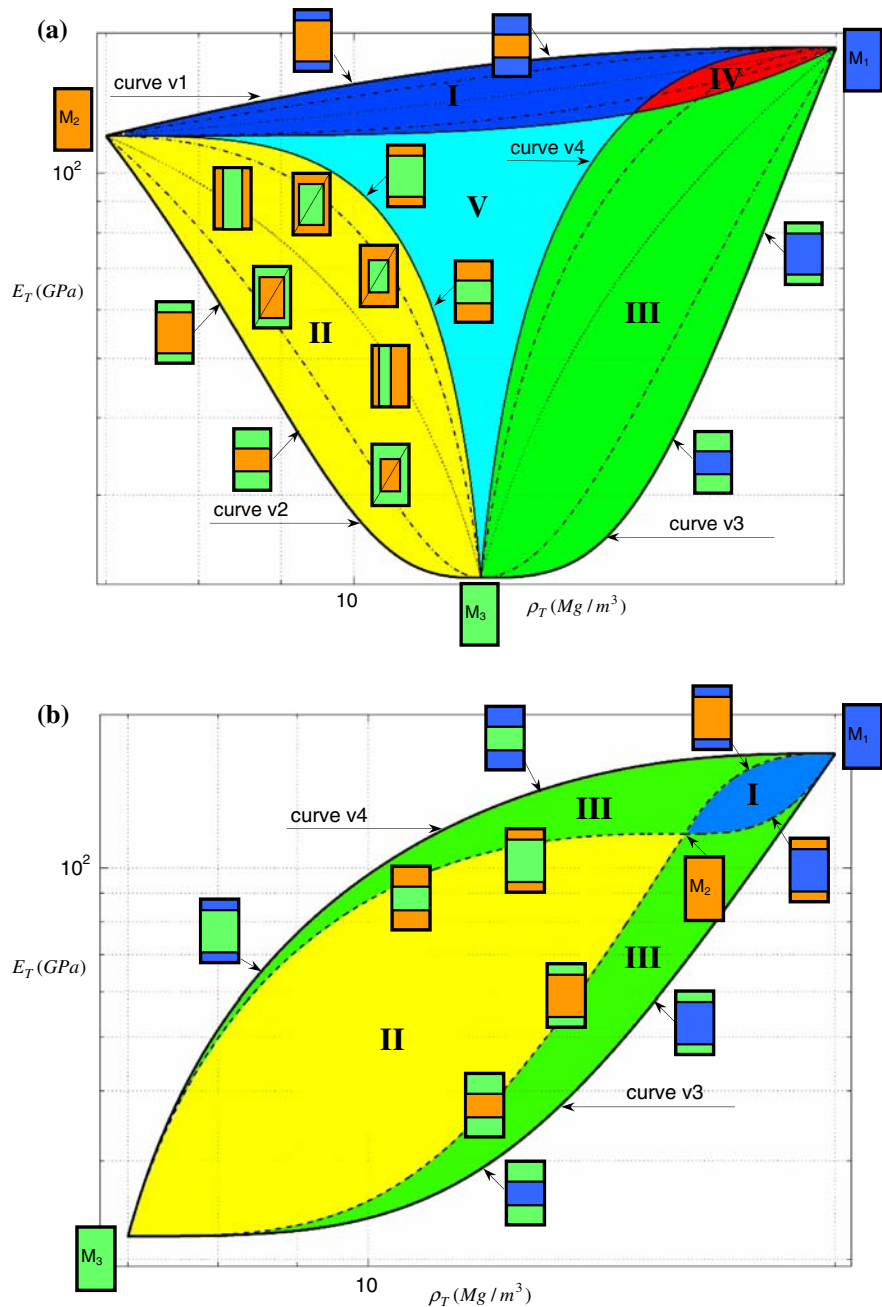
Material	$E$ (GPa)	$\rho$ (mg/m <sup>-3</sup> )
SiC	400	3.2
Si	160	2.3
ZrO <sub>2</sub>	110	6.5
Si <sub>3</sub> N <sub>4</sub>	185	3.5
GaAs	82	5.2
Ag	92	10.2
Quartz	110	2.65
Ti	120	4.5
Ni	200	8
Quartz	110	7.5
Cu	120	8.9

materials attributes plotted in the charts are the bulk density and Young's Modulus. Extensive experimental measurements showed that nominal bulk material properties (Table 3) can be used at the early design stage as conservative figures in place of the real microstructural material properties (Sharpe 2001). If expressions (8) and (9) with data from Tables 1, 2 and 3 are plotted, then the system evolutions shown in Fig. 1 can be examined. Figure 5a, b represent the properties of a rectangular multilayered system for a given scenario. Each of them is determined by the relative values of three constituent materials  $M_1$  ( $\rho_1, E_1$ ),  $M_2$  ( $\rho_2, E_2$ ) and  $M_3$  ( $\rho_3, E_3$ ).

- The first scenario is depicted in Fig. 5a and it emerges when  $M_2$  has properties falling outside the area defined by curve v3 and v4 of the bi-material  $M_1$ – $M_3$ . In this case, the overall domain consists of five sub-domains and it contains all the possible configurations based on the three materials arranged in multiple layers either symmetrically or asymmetrically about the envelope axes. Domains I, II, and III refer to the bi-material systems, namely  $M_1$ – $M_2$ ,  $M_2$ – $M_3$ ,  $M_1$ – $M_3$ ; they describe sandwich concepts, which have been demonstrated to have specific property bounds. Within them, there exist all the possible bi-material systems containing two, three, five, seven and multiple layers arranged either symmetrically or asymmetrically about the envelope mid-plane (Pasini 2006a). Domain IV describes properties that can be achieved by either the bi-material

**Fig. 5 a** The five sub domains for a three material system with  $E_3 < E_2 < E_1$  and  $\rho_2 < \rho_3 < \rho_1$ .  $M_1$  ( $\rho_1 = 20$ ,  $E_1 = 160$ ), and  $M_2$  ( $\rho_2 = 7$  mg/m<sup>3</sup>,  $E_2 = 115$  GPa), and  $M_3$  ( $\rho_3 = 12$ ,  $E_3 = 80$ ). Dash-dot lines for proportionally scaled layers class, dot lines for horizontally scaled layers, continuous lines for vertically scaled layers.

**b** The three sub domains of a three material system with  $E_3 < E_2 < E_1$  and  $\rho_3 < \rho_2 < \rho_1$ .  $M_1$  ( $\rho_1 = 20$ ,  $E_1 = 160$ ),  $M_2$  ( $\rho_2 = 12$ ,  $E_2 = 115$ ) and  $M_3$  ( $\rho_3 = 7$ ,  $E_3 = 80$ ). Hidden lines for vertically scaled layers of the bi-material  $M_2$ – $M_3$  and  $M_1$ – $M_2$  systems; continuous lines for vertically scaled layers of the bi-material  $M_1$ – $M_3$  system



systems  $M_1$ – $M_2$  and  $M_1$ – $M_3$  or the tri-material system  $M_1$ – $M_2$ – $M_3$ . Domain V, on the other hand, pertains to systems necessarily composed of three materials, i.e. all three constituents are to be integrated. Within the sub-domains, different line-styles are used to differentiate among shape classes, as shown for the bi-material  $M_2$ – $M_3$ .

- The second scenario occurs when  $(\rho_2, E_2)$  falls within the bi-material domain  $M_1$ – $M_3$ . As shown in Fig. 5b, three sub-domains emerge. In contrast to the previous scenario, this time the overall domain is bounded by the limiting curves of the bi-material domain  $M_1$ – $M_3$ , curves v3 and v4. A region similar to sub-domain V in Fig. 5a does not appear in

Fig. 5b. Thus, adding a third material does not have the effect of expanding the tri-material properties space. Rather the overlapping regions illustrate that alternative concepts are equivalent in performance. This means that the properties of all the possible tri-material system can also be achieved by at least one of the other three bi-materials. The outcome is relevant to micro-structure design when material availability, manufacturing issues and cost are to be considered.

### 5.1 Maps for systems with vertically scaled layers

In this section, we look closer at the class of the vertically scaled layers and examine the evolutions depicted in Fig. 1 from a to d. The first two are governed by the constraint  $V_1 = \text{const}$ ; the others by  $V_1/V_2 = \text{const}$ .

As an example, we initially choose a bi-material  $M_1$ – $M_2$  with a  $M_2$  volume fraction of 16%, as illustrate by point A in Fig. 6a. When a third material layer  $M_3$  of Young's modulus lower than the other two, i.e.  $E_3 < E_2 < E_1$ , of increasing thickness are added as a middle layer (Fig. 1a), while  $V_2$  is constrained to 16%, a progressive reduction of both the total density and stiffness is obtained. This is shown by the downward arrow on the upper curve A–B, which is governed by a cubic relation. However, although the effective properties reduce, the integration of a lower Young's modulus material increases the overall performance  $E_T/\rho_T$ . The performance continues to improve until the three-material reaches point B, where  $M_3$  replaces  $M_2$  and the system has become a bi-material containing 74% of  $M_3$ . Similar reasoning applies to describe the flexural modulus of the evolution shown in Fig. 1b. Stiffer  $M_3$  layers are added in the middle of the configuration shown by B. This time a corresponding change in the volume fraction of the respective materials transforms the properties from B to A, following upward the lower curve.

The second constraint imposes the volume fraction  $V_1/V_2$  of the inner material layers to be constant during the system evolution. As an example, the starting bi-material system in Fig. 1c is chosen to have  $V_1/V_2 = 55\%$  and its flexural modulus is illustrated by point C. When an increasing thickness layer of a softer material  $M_3$  is added in the middle,

the system then evolves progressively until the volume fraction of  $M_1$  and  $M_2$  reaches zero, i.e. point D. Here, the system is monolithic and its flexural modulus consists a 100% of  $M_3$ . The flexural modulus, which describes the system evolution for progressive changes of volume fraction of the respective materials, is shown by the upper curve CD in Fig. 6b. This concept is particular because during evolution the constraint  $V_1/V_2 = \text{const}$  has the effect of stiffening the system although a softer material is integrated. The maximum bending stiffness is reached at E, where the volume fraction of  $M_3$  is 30%. Then, the stiffness reduces progressively, although  $E_T/\rho_T$  increases until  $\rho_T \rightarrow \rho_3$ .

### 5.2 Maps for proportionally scaled layer systems

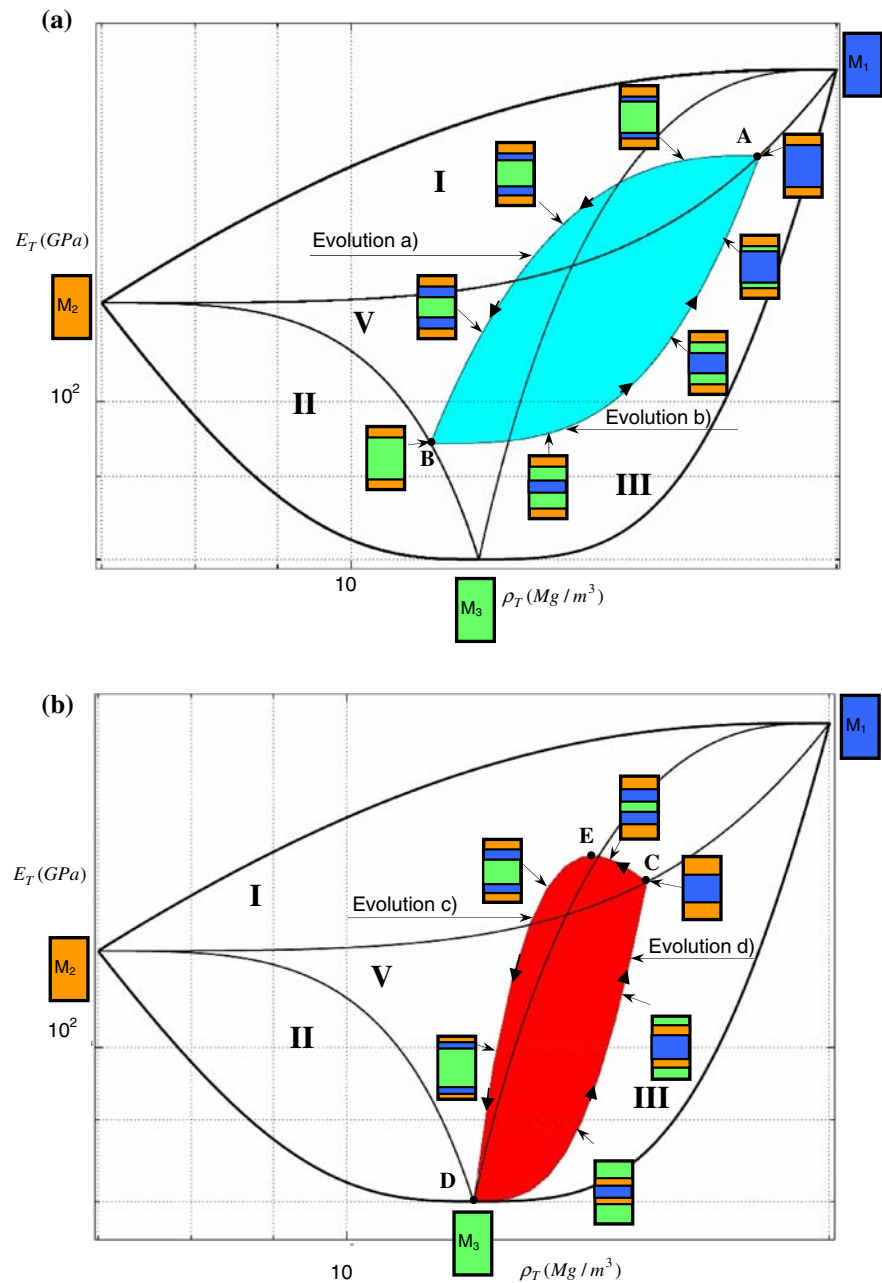
Figure 7a, b show the domain of the class of the proportionally scaled layers and the change of flexural modulus for the system evolution illustrated in Fig. 1e, f. Similar to those in Fig. 1a, b, these sequences pertain to the constraints  $V_1 = \text{const}$  and  $V_1/V_2 = \text{const}$ .

Compared to the vertically scaled layers class, here the overall domain for both constraints shrinks and the bounds are governed by quadratic relations, i.e. curves FG and HD. It can be observed that the effect of each constraint on the flexural modulus resembles that exhibited by the class of the vertically scaled layers.

The flexural modulus of the starting bi-material shown in Fig. 1e is represented in Fig. 7a by point F, which is chosen, as an example, to have  $V_2 = 49\%$ . With respect to the shape classes, increasing the thickness of material  $M_3$  in the middle reduces the flexural modulus following downward the upper curve FG until point G, where  $M_2$  has completely replaced  $M_1$  with a volume fraction of 51%. Likewise, when a stiffer layer is added in the middle of system G, the flexural modulus is visualized by the lower curve GF.

In Fig. 7b, the flexural modulus is plotted for the evolution f) in Fig. 1 where  $V_1/V_2$  is constrained to 0.55. This constraint has also a particular effect on the flexural modulus of this shape class. Adding a softer material increases the stiffness of the system until the bending stiffness reaches the maximum at point I, where the volume fraction of  $M_3$  is 16%.

**Fig. 6** **a** The curves of the shaded sub-domain describes the tri-material evolutions shown in Fig. 1a and b for vertically scaled layers with a volume percentage of  $M_2$  constrained to 16%. The limiting bi-material configurations, i.e. points A and B, contain 74% volume fraction of  $M_1$  and  $M_3$ , respectively. **b** The curves of the shaded sub-domain describe the tri-material evolutions shown in Fig. 1a, b for vertically scaled layers with volume ratio  $V_1/V_2$  constrained to 55%. The limiting bi-material configuration C contains 45% of  $M_2$ , whereas D has a volume fraction of 100% of  $M_3$ . Point E contains 30% volume fraction of  $M_3$



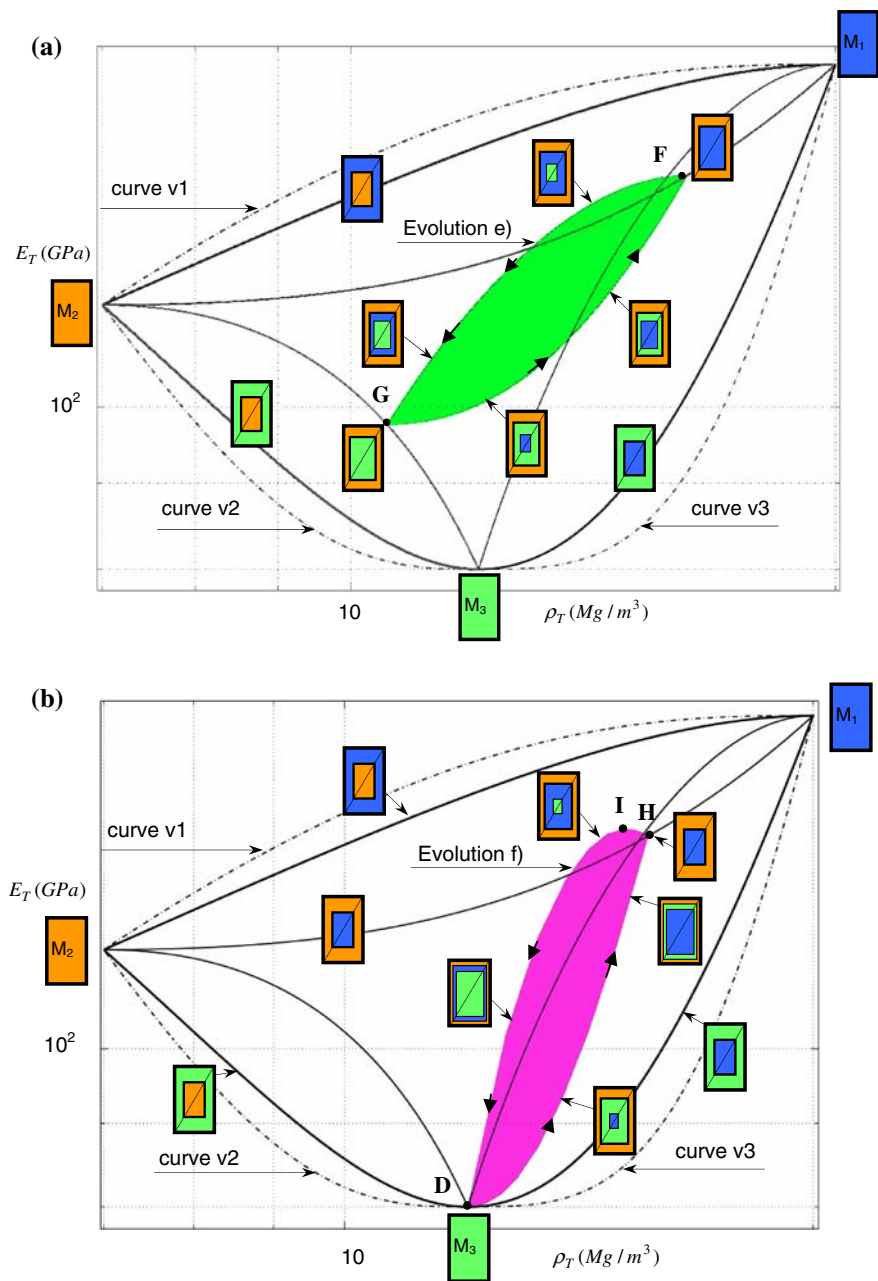
### 5.3 Maps for horizontally scaled layer systems

For the class of the horizontally scaled layers consisting of two materials, symmetry and number of laminates have no effect on  $E_T/\rho_T$  (Pasini 2006a). Figure 8 shows a similar behaviour also for the evolution of a tri-material system. The linear relation governing the effective properties has the effect of

reducing the domains to lines ( $M_1$ – $M_2$ ;  $M_1$ – $M_3$ ;  $M_2$ – $M_3$ ) irrespective of the number and symmetry of layers. The evolutions shown in Fig. 1g and f also reduce to lines LM and ND for the two constraints. When  $V_1/V_2 = \text{const}$ , the gradient of the line is greater than the case for  $V_1 = \text{const}$ . This time, in contrast to the other shape classes, no increase in stiffness is observed when a softer material is integrated into the system.



**Fig. 7** **a** The curves of the shaded sub-domain describes the tri-material evolutions shown in Fig. 1e) for proportionally scaled layers with a constrained volume percentage of 49% for  $M_2$ . For the limiting bi-material configurations, F and G contain respectively 51% volume fraction of  $M_1$  and of  $M_3$ . **b** The curves of the shaded sub-domain describe the tri-material evolutions shown in Fig. 1f) for proportionally scaled layers with volume ratio  $V_1/V_2$  constrained to 0.55. For the starting bi-material configuration, H contains 51% of  $M_1$  and 49% volume fraction of  $M_2$ ; I contains 16% of the volume fraction of  $M_3$

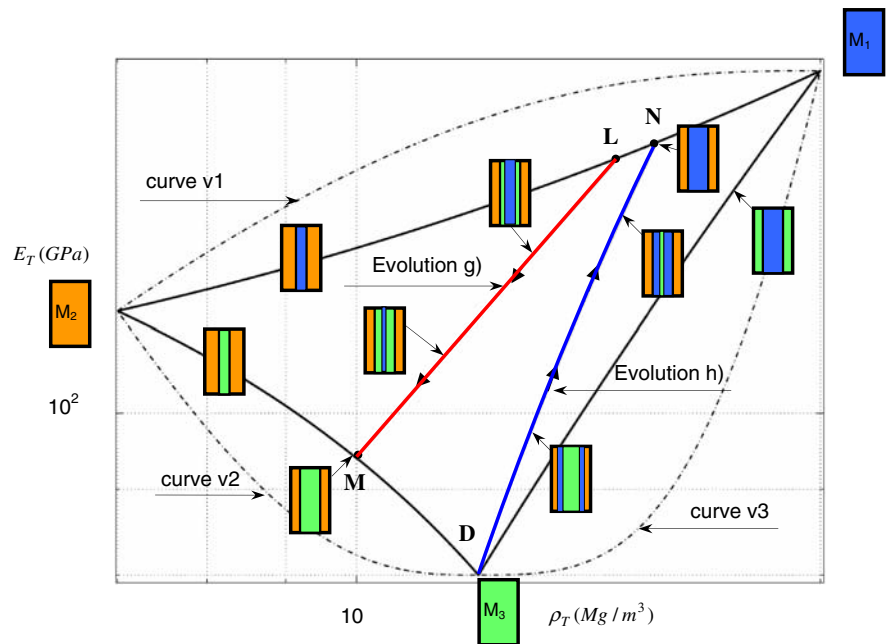


## 6 Case study on the use of the map $E_T$ vs. $\rho_T$ for the selection of structural concepts

The aim of this section is to illustrate the benefit of using this method for the design of multilayered structures. The functional requirements of a micro-device and the manufacturing process used to shape it into a selected configuration govern the choice of one

or a combination of materials. The model described in this article is grounded on the mechanical characterization of the flexural properties of a micro-beam; the maps are a tool that assists the preliminary design because they ease the simultaneous scrutiny of structural design alternatives. However for the final choice, other important factors, such as the constraints imposed by different fabrication technologies as well

**Fig. 8** The lines LM and DN describe the tri-material evolutions shown in Fig. 1g, h for horizontally scaled layers, respectively with  $V_2 = 40\%$  and volume ratio  $V_1/V_2 = 0.55$ . For initial bi-material configurations, L contains 60% volume fraction of  $M_1$  and 40% volume fraction of  $M_2$ ; M contains 60% volume fraction of  $M_3$  and 40% volume fraction of  $M_2$



as their associated cost, need to be taken into account. Further research is required to include such limits into the maps.

This section illustrates a comparative study of structural concepts that differ for materials, cross-section geometry, layer architecture, and number of constituent materials. The problem deals with the comparison and selection of structural concepts for a vibrating micro-cantilever beam; the maps are developed for screening alternatives and for filtering the one that optimizes the vibration frequency. All four scenarios are considered here in unconstrained and constrained design. In the first case, no restrictions are applied to the beam geometry; whereas in the other three cases, either the width or the height or both are prescribed. The following structural concepts are considered:

- (1) a three-material prismatic system, which consists of Silicon (Si), Silicon Carbide (SiC), and Zirconium Oxide ( $\text{ZrO}_2$ );
- (2) a bi-material rectangular compound of Silicon Nitride ( $\text{Si}_3\text{N}_4$ ) and Gallium Arsenide (GaAs);
- (3) a bi-material circular (or elliptical) system with proportionally scaled layers of Silicon and Silver (Ag);
- (4) a bi-material structure with vertically scaled layers of Copper (Cu) and Silver;

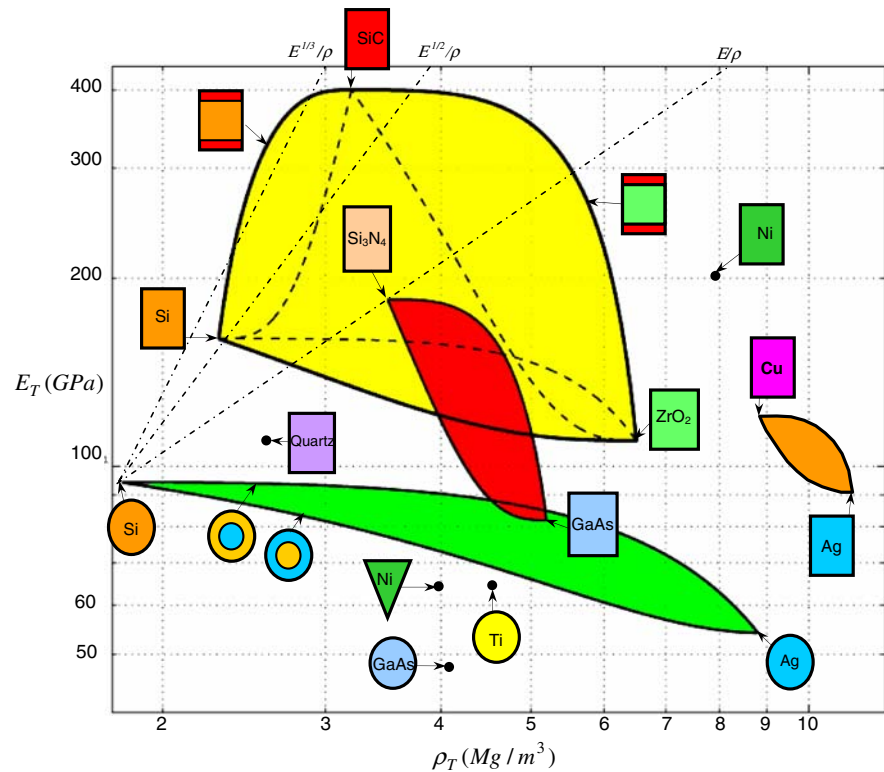
- (5) two solid prismatic beams respectively of Quartz and Nickel (Ni);
- (6) two solid cylindrical cantilevers; one made out of Titanium (Ti) and the other of GaAs;
- (7) a solid triangular cross-section structure of Nickel.

Figure 9 shows all together the flexural properties of the candidates. The plot was obtained by using the shape transformer expressions (Tables 1 and 2) and their material properties (Table 3). Whereas properties domains emerge for planar systems containing either two or three materials, the properties of solid monolithic structures are identified by single points.

- For bi-material systems, the domain boundaries describe the change of the flexural modulus when the volume fraction changes. The upper curves identify systems where the coating material is stiffer, as opposed to the lower bounds, which represent stiff core bi-materials. The curves describe the vertically scaled layer class of the rectangle family for Cu-Ag,  $\text{Si}_3\text{N}_4$ -GaAs, and the proportionally scaled layer class of the elliptical family for Si-Ag.
- For the three-material system, five sub-domains, similar to those depicted in Fig. 5, emerge. The major domain is bounded by the three bold



**Fig. 9** Design map for selection of alternative vibrating micro-structures



continuous lines and within it fall all the bi- and tri-material systems of the rectangles family with two, three, and multiple, layers arranged symmetrically and asymmetrically about the envelope mid-plane (Pasini 2006a). As demonstrated previously, constraining the volume fraction  $V_1$  or  $V_1/V_2$  results in system evolutions characterized by flexural properties curves which, albeit significantly different, lie always inside the general domain.

For concept selection, besides properties domains selection guidelines are to be plotted on a map. If relations (10), (12), (13), (14) are recast into the form of expression (15) and plotted as selection lines, then several insights are revealed. For example in Fig. 9, if the lines are set on the beam with solid elliptical cross-section made out of Si, then the candidates can be easily ranked for each scaling condition. As can be seen, a scaling constraint strongly impacts the ranking of the structural concepts. The systems laying above a line show that shaping Si-SiC-ZrO<sub>2</sub> into a planar system of the rectangular family can provide higher flexural vibrations for certain volume

fractions of the materials layered into a given layout. The intersections of each line with the domain boundaries determine the thresholds of the volume fraction for the best design concept under given constraints.

Another feature of Fig. 9 involves the domain overlaps emerging by the intersection of regions from different concepts. For example, Si<sub>3</sub>N<sub>4</sub>-GaAs partly covers the domains of Si-SiC-ZrO<sub>2</sub> and Si-Ag. This outcome highlights that there are different concepts that provide the same flexural properties and vibration performance, a feature of relevance when material availability and other functional requirements might induce the search for an alternative design.

Validating the method presented in this article is essential to the design of microstructures. The model is governed by the classic laminated plate theory and the Euler-Bernoulli theory, recently verified both numerically and experimentally (Sader 1998; Serre et al. 1999; Rasmussen et al. 2003; Jennifer et al. 2004; Lin 2004b; Ferguson et al. 2005; Sandberg et al. 2005a, b, c; Mertens et al. 2003; Melamud et al. 2006; Wang et al. 2000; Prasanna and Spearing

2007). These studies for single and multilayered microstructures set the validity boundaries of the results given in this article, because they demonstrate the predictions diverge no more than 3% from experiment measures. Reasons for such a deviation include anchor dissipation and boundary conditions, uncertain measures of thicknesses and material properties.

The scheme proposed here enables the visualization of properties bounds for alternative concepts and is conducive to optimize performance at the concept stage, where each structural alternative is described by its own set of design variables and can be contrasted for different design scenarios.

## 7 Conclusions

The evolution of a multi-layered micro-system consisting of three dissimilar materials has been examined by constraining the volume fraction to specific values. Flexural stiffness domains have been determined for different layer architectures of a tri-material laminate system. It has been demonstrated that a bi-material sandwich system can be stiffened by adding layers of a more flexible material while constraining the volume fraction ratio of constituent materials. The scheme presented in this article captures the impact of structural variables for laminate materials, layer architecture and cross-section geometry. Maps for concept design have been developed to ease the visual ranking of alternatives and contrast the flexural properties of multi-material systems with monolithic structures of different cross-section geometries.

It is anticipated that this method can be used to model other mechanical properties relevant to the design of micro-devices.

## References

- Ashby, M.F.: Materials and shape. *Acta Metall. Mater.* **39**(6), 1025–1039 (1991). doi:[10.1016/0956-7151\(91\)90189-8](https://doi.org/10.1016/0956-7151(91)90189-8)
- Ashby, M.F.: Criteria for selecting the components of composites. *Acta Metall. Mater.* **41**(5), 131–135 (1993a). doi:[10.1016/0956-7151\(93\)90242-K](https://doi.org/10.1016/0956-7151(93)90242-K)
- Ashby, M.F.: Criteria for selecting the components of composites. *Acta Metall. Mater.* **41**(5), 131–135 (1993b). doi:[10.1016/0956-7151\(93\)90242-K](https://doi.org/10.1016/0956-7151(93)90242-K)
- Ashby, M.F.: Material Selection in Mechanical Design. Pergamon Press, Oxford (1999)
- Caldwell, J.B., Woodhead, R.G.: Ship structures: some possibilities for improvement. *Transactions of North East Coast Institution of Engineers and shipbuilders* **89**, 101–120 (1973)
- Cheggour, N., Ekin, J.W., Thieme, C.L.H., Xie, Y.-Y., Selva-manickam, V., Feenstra, R.: Reversible axial-strain effect in Y–Ba–Cu–O coated conductors. *Supercond. Sci. Technol.* **18**(12), S319–S324 (2005). doi:[10.1088/0953-2048/18/12/016](https://doi.org/10.1088/0953-2048/18/12/016)
- Cox, H.L.: The design of structures of least weight. Pergamon Press, Oxford (1965)
- Degani, O., Seter, D.J., Socher, E., Kaldor, S., Nemirovsky, Y.: Optimal design and noise consideration of micro machined vibrating rate gyroscope with modulated integrative differential optical sensing. *J. Microelectromech. Syst.* **7**, 329–338 (1998). doi:[10.1109/84.709652](https://doi.org/10.1109/84.709652)
- de Silva, C.W.: Sensors and Actuators: Control System. CRC Press, Boca Raton, FL (2007)
- Ferguson, A.T., Li, L., Nagaraj, V.T., Balachandran, B., Piekarski, B., DeVoe, D.L.: Modeling and design of composite free-free beam piezoelectric resonators. *Sens. Actuators* **118**(1), 63–69 (2005). doi:[10.1016/S0924-4247\(04\)00540-0](https://doi.org/10.1016/S0924-4247(04)00540-0)
- Gad-el-Hak, M.: The MEMS Handbook, II edn. CRC Press, Boca Raton, FL (2002)
- Galayko, D., Kaiser, A., Legrand, B., Buchallot, L., Collard, D., Combi, C.: Tunable bandpass T-filter with electrostatically-driven polysilicon micromechanical resonators. *Sens. Actuators A Phys.* **117**, 115–120 (2005). doi:[10.1016/j.sna.2004.06.002](https://doi.org/10.1016/j.sna.2004.06.002)
- Hong, Y.S., Lee, J.H., Kim, S.H.: A laterally driven symmetric micro-resonator for gyroscopic applications. *J. Micro-mech. Microeng.* **10**, 452–458 (2000). doi:[10.1088/0960-1317/10/3/322](https://doi.org/10.1088/0960-1317/10/3/322)
- Huang, X.M.H., Ekin, K.L., Yang, Y.T., Zorman, C.A., Mehregany, M., Roukes, M.L.: Nanoelectromechanical silicon carbide resonators for ultra-high frequency applications. In: *Proceedings of the 2002 Sensor, Actuator and Microsystems Workshop*, Hilton Head, SC, 2–6 June 2002, pp. 368–369
- Huber, J.E., Fleck, N.A., Ashby, M.F.: The selection of mechanical actuators based on performance indices. *Proc. R. Soc. Lond. A* **453**, 2185–2205 (1997)
- Jennifer, W.L.Z., Chan, H.-Y., To, T.K.H., Lai, K.W.C., Li, W.J.: Polymer MEMS actuators for underwater micro-manipulation. *IEEE/ASME Trans. Mechatron.* **9**(2), 334–342 (2004). doi:[10.1109/TMECH.2004.828652](https://doi.org/10.1109/TMECH.2004.828652)
- Khaled, A.-R.A., Vafai, K., Yang, M., Zhang, X., Ozkan, C.S.: Analysis, control and augmentation of microcantilever deflections in bio-sensing systems. *Sens. Actuators* **94**, 103–115 (2003). doi:[10.1016/S0925-4005\(03\)00231-4](https://doi.org/10.1016/S0925-4005(03)00231-4)
- Lange, D., Hagleitner, C., Herzog, C., Brand, O., Baltes, H.: Magnetic actuation and MOS-transistor sensing for CMOS-integrated resonators. In: *15th IEEE International Conference on Micro-Electro Mechanical Systems, MEMS 2002*, Las Vegas, Nevada, USA, 20–24 January 2002, pp. 304–307
- Lin, S.: Effect of electric load impedances on the performance of sandwich piezoelectric transducers. *IEEE Trans.*

- Ultrason. Ferroelectr. Freq. Control. **51**(10), 864–869 (2004a)
- Lin, S.: Piezoelectric ceramic rectangular transducers in flexural vibration. IEEE Trans. Ultrason. Ferroelectr. Freq. Control. **51**(7), 1280–1286 (2004b)
- Marie, R., Jensenius, H., Thaysen, J., Christensen, C.B., Boisen, A.: Adsorption kinetics and mechanical properties of thiol-modified DNA-oligos on gold investigated by microcantilever sensors. Ultramicroscopy **91**, 29–36 (2002). doi:[10.1016/S0304-3991\(02\)00079-7](https://doi.org/10.1016/S0304-3991(02)00079-7)
- Melamud, R., Kim, B., Hopcroft, M.A., Chandorkar, S., Agarwal, M., Jha, C., Bhat, S., Park, K.K., Kenny, T.W.: Composite flexural mode resonator with reduced temperature coefficient of frequency. In: Solid-State Sensors, Actuators, and Microsystems Workshop, South Carolina, 4–8 June 2006
- Mertens, J., Finot, E., Thundat, T., Fabre, A., Nadal, M.-H., Eyraud, V., Bourillot, E.: Effects of temperature and pressure on microcantilever resonance response. Ultramicroscopy **97**(1), 119–126 (2003). doi:[10.1016/S0304-3991\(03\)00036-6](https://doi.org/10.1016/S0304-3991(03)00036-6)
- Nguyen, C.T.-C.: Micromechanical resonators for oscillators and filters. In: Proceeding 1995 IEEE International Ultrasonic Symposium Seattle, WA, USA (1995)
- Nguyen, C.T.-C., Katehi, L.P.B., Rebeiz, G.M.: Micromachined devices for wireless communications. Proc. IEEE. **86**, 1756–1768 (1998). doi:[10.1109/5.704281](https://doi.org/10.1109/5.704281)
- Nguyen, C.T.-C.: Frequency-selective MEMS for miniaturized low-power communication devices. IEEE. Trans. Microw. Theory Tech. **47**(8), 1486–1503 (1999)
- Nguyen, C.T.-C.: Vibrating RF MEMS for next generation wireless applications. In: Proceedings of the 2004 IEEE Custom Integrated Circuits Conference, Orlando, Florida, 3–6 October 2004, pp. 257–264
- Parkhouse, J.G.: Structuring a process of material dilution. In: Nooshin, H. (ed.) Proceedings of the 3rd International Conference on Space Structures, pp. 367–374. Elsevier Applied Science Publishers, New York (1984)
- Pasini, D.: Material and shape selection for optimizing flexural vibrations in multilayered resonators. J. Microelectromech. Syst. **15**(6), 1745–1758 (2006a). doi:[10.1109/JMEMS.2006.885997](https://doi.org/10.1109/JMEMS.2006.885997)
- Pasini, D.: Shape transformers for material and shape selection of lightweight beams. J. Mater. Des. **28**(7), 2071–2079 (2006b)
- Pasini, D., Smith, D.J., Burgess, S.C.: Structural efficiency maps for beams subjected to bending. Proc. Instn Mech. Engrs, Part L. J. Mater. Des. Appl. **217**(3), 207–220 (2003)
- Prasanna, S., Spearing, S.M.: Materials selection and design of microelectrothermal bimaterial actuators. J. Microelectromech. Syst. **16**(2), 248–259 (2007). doi:[10.1109/JMEMS.2006.889528](https://doi.org/10.1109/JMEMS.2006.889528)
- Rakshit, S., Ananthasuresh, G.K.: Simultaneous material selection and geometry design of statically determinate trusses using continuous optimization. J. Struct. Multidiscip. Optim. **35**(1), 55–68 (2008). doi [10.1007/s00158-007-0116-4](https://doi.org/10.1007/s00158-007-0116-4)
- Rasmussen, P.A., Thaysen, J., Hansen, O., Eriksen, S.C., Boisen, A.: Optimised cantilever biosensor with piezoresistive read-out. Ultramicroscopy **97**(1), 371–376 (2003). doi:[10.1016/S0304-3991\(03\)00063-9](https://doi.org/10.1016/S0304-3991(03)00063-9)
- Sader, J.E.: Frequency response of cantilever beams immersed in viscous fluids with applications to the atomic force microscope. J. Appl. Phys. **84**, 64–76 (1998). doi:[10.1063/1.368002](https://doi.org/10.1063/1.368002)
- Sandberg, R., Boisen, A., Svendsen, W.: Characterization system for resonant micro- and nanocantilevers. Rev. Sci. Instrum. **76**, 125101 (2005a)
- Sandberg, R., Mølhave, K., Boisen, A., Svendsen, W.: Effect of gold coating on the *Q*-factor of a resonant cantilever. J. Micromech. Microeng. **15**, 2249–2253 (2005b). doi: [10.1088/0960-1317/15/12/006](https://doi.org/10.1088/0960-1317/15/12/006)
- Sandberg, R., Svendsen, W., Mølhave, K., Boisen, A.: Temperature and pressure dependence of resonance in multilayer microcantilevers. J. Micromech. Microeng. **15**, 1454–1458 (2005c). doi:[10.1088/0960-1317/15/8/011](https://doi.org/10.1088/0960-1317/15/8/011)
- Senturia, S.D.: Microsystem Design. Kluwer, Norwell, MA (2001)
- Serre, C., Perez-Rodriguez, A., Morante, J.R., Gorostiza, P., Esteve, J.: Determination of micromechanical properties of thin films by beam bending measurements with an atomic force microscope. Sens. Actuators **74**, 134–138 (1999). doi:[10.1016/S0924-4247\(98\)00347-1](https://doi.org/10.1016/S0924-4247(98)00347-1)
- Shanley, F.R.: Weight–strength Analysis of Aircraft Structures, 2nd edn. New York, Dover (1960)
- Sharpe, W.N.: Mechanical properties of MEMS materials, chapter 3. In: Gad-el-Hak, M. (ed.) The MEMS Handbook, pp. 3–33. CRC Press, Boca Raton, FL (2001)
- Shieh, J., Huber, J.E., Fleck, N.A., Ashby, M.F.: The selection of sensors. Prog. Mater. Sci. **46**, 461–504 (2001). doi: [10.1016/S0079-6425\(00\)00011-6](https://doi.org/10.1016/S0079-6425(00)00011-6)
- Smith, D.J., Partbridge, P.G.: Flexural stiffness envelopes for planar system containing two dissimilar materials. Proc. Instn Mech. Engrs, Part L. J. Mater. Des. Appl. **213**, 1–20 (1999)
- Sova, M., Bogdan, I.: Coplanar waveguide resonator design for array antenna applications. In: 6th International Conference on Telecommunications in Modern Satellite, Cable and Broadcasting Service, vol. 1, pp. 57–59. Las Alamos, USA (2003)
- Spaepen, F.: Interfaces and stresses in thin films. Acta Mater. **48**(1), 31–42 (2000). doi:[10.1016/S1359-6454\(99\)00286-4](https://doi.org/10.1016/S1359-6454(99)00286-4)
- Spearing, S.M.: Materials issues in microelectromechanical systems (MEMS). Acta Mater. **48**, 179–196 (2000). doi: [10.1016/S1359-6454\(99\)00294-3](https://doi.org/10.1016/S1359-6454(99)00294-3)
- Taka, A.M., Omodaka, A., Takeshima, N., Fujita, H.: Fabrication and operation of polyimide bimorph actuators for a ciliary motion system. J. Microelectromech. Syst. **2**, 146–150 (1993)
- Thaysen, J., Yalcinkaya, A.D., Vettiger, P., Menon, A.: Polymer-based stress sensor with integrated readout. J. Phys. D Appl. Phys. **35**, 2698–2703 (2002). doi:[10.1088/0022-3727/35/21/302](https://doi.org/10.1088/0022-3727/35/21/302)
- Vengallatore, S., Spearing, S.M.: Materials selection for microfabricated electrostatic actuators. Sens. Actuators **102A**, 279–285 (2003)
- Wang, W., Soper, S.A.: Bio-MEMS; Technologies and Applications. CRC Press, Boca Raton, FL (2006)
- Wang, K., Wong, A.-C., Nguyen, C.T.-C.: VHF free–free beam high-*Q* micromechanical resonators. J. Microelectromech. Syst. **9**(3), 347–360 (2000). doi:[10.1109/84.870061](https://doi.org/10.1109/84.870061)

- Wong, A.C., Nguyen, C.T.-C.: Micromechanical mixer-filters. *J. Microelectromech. Syst.* **13**, 100–112 (2004). doi: [10.1109/JMEMS.2003.823218](https://doi.org/10.1109/JMEMS.2003.823218)
- Yang, G.H., Chen, J.B., Pan, F.: The effects of layer thickness on the microstructure and magnetic properties of evaporated Co/Ag films. *Phys. Status Solidi A* **194**(1), 71–80 (2002)
- Yue, M., Lin, H., Dedrick, D.E., Satyanarayana, S., Majumdar, A., Bedekar, A.S., Jenkins, J.W., Sundaram, S.: A 2-D microcantilever array for multiplexed biomolecular analysis. *J. Microelectromech. Syst.* **13**, 290–299 (2004). doi: [10.1109/JMEMS.2003.823216](https://doi.org/10.1109/JMEMS.2003.823216)